RESEARCH ARTICLE

ADVANCED MATERIALS TECHNOLOGIES
www.advmattechnol.de

Reusable, Fully Integrated Sweat Monitor Band with Peel-and-Stick-Replacement Printed Microfluidic Sensor

*Noelle Davis, Amanda Kang, Elina Hakola, Liam Gillan, Yifei Zhan, Jussi Hiltunen, and Ali Javey**

This paper presents a continuous monitor for local sweat rate consisting of a fully reusable, wearable band with an integrated electronics module and a disposable, peel-and-stick-replacement microfluidic sensor with printed electrodes. Local sweat rate sensors on specific skin sites have the potential to inform hydration strategies, with many devices recently introduced in the academic domain and even a few in the commercial domain. Here, several challenges in the design of sweat sensing systems are addressed: high reusability with minimal single-use material, robust interfacing with the single-use component in both electrical and fluidic pathways, implementation of scalable, roll-to-roll screen printing processes, and integration of precise measurements with continuous, wireless readout. Finally, the device is demonstrated on-body during environmental heat and cycling exercise. In the near future, it is expected that this device will enable the academic study of sweat rate, and eventually, help make this biometric accessible to those such as workers and athletes in harsh environments.

1. Introduction

Sweating is a unique physiological phenomenon that plays a key role in human thermoregulation and hydration, especially under physically demanding conditions. Local sweat rate from the forearm and other skin sites has been shown across many subjects to correlate well with whole-body fluid loss,[1] validating the pursuit of a wearable device for real-time estimations of this dehydration metric.

This paper builds on a volumetric sweat rate sensing mechanism described in previous work,[2,3] and advances aspects of the system beginning with the microfluidic and electrical interfaces. Here, we validate a peel-and-stick fluidic interface over numerous replacements, as well as an electrical interface with spring-loaded pins and magnetic closure to integrate the printed sensor with custom onboard electronics. As a result, the single-use component of the system, the microfluidic sensor, is simple and inexpensive via roll-to-roll (R2R) processing, and the rest of the device is fully reusable. Further, ease of sensor replacement allows for rapid sensor replacement mid-activity, enabling prolonged measurements with the precision of volumetric sensing. Although distinct from sensor technology development, packaging design is a critical element of wearable sensor systems research. Recent wearable microfluidic sweat sensors have commonly taken one of two form factors: a patch adhered to the skin[4,5] and a nonadhesive collector pressed against the skin by a band,[2,6,7] which can be worn on the arm or other limb and possibly even integrated with a smartwatch. Considerations for the form factor include user experience, measurement quality, and reusability. A form factor that is unobtrusive and comfortable has a higher likelihood of user adoption and a lower chance of mechanical disturbance during wear. For example, a band-based device integrated with a smartwatch poses little added interference to the user. The form factor also has an impact on sensor measurements. Due to applied pressure, a band-based microfluidic device can have more conformal contact with the skin collection area than an adhesive-based microfluidic device. While this may involve temporary skin deformation, it can also enable a lower dead volume and less initial lag time for measurements. Here, we have built on a design for a wearable band with a semi-soft, concave skin-side interface optimized for low dead volume.[2] Another consideration is plastic waste from single-use disposable components. Designing with the mechanical structure of a band enables us to limit the disposable component to a thin sticker.

Other packaging challenges include enforcing robust connections in both fluidic and electrical pathways, especially at the interfaces of reusable and disposable subsystems of a device. The division into these subsystems addresses the fundamental issue of sensor contamination, arising from the corrosivity of salt and biofouling propensity of proteins and lipids, but requires fluidic and electrical interfaces to support many connection cycles. Alternatives to a disposable sensor component include isolation between sample and sensor and use of a cleaning procedure

---

N. Davis, A. Kang, Y. Zhan, A. Javey
University of California
Berkeley, CA 94720, USA
E-mail: ajavey@berkeley.edu

E. Hakola, J. Hiltunen
VTT Technical Research Centre of Finland
Oulu 90590, Finland

L. Gillan
VTT Technical Research Centre of Finland
Espoo 02150, Finland

The ORCID identification number(s) for the author(s) of this article can be found under https://doi.org/10.1002/admt.202500477

DOI: 10.1002/admt.202500477

between measurements, but in any case, the issue of contamination affects all sweat sensing systems with a sensing channel or chamber inhabited by sweat, across different sensing mechanisms–whether volumetric,[2] calorimetric (using heat transfer to measure fluid flow rate),[8] or hygrometric.[9] Considering the approach of separate reusable and disposable subsystems, fluidic interfaces must have adhesion strong enough to prevent leakage and mild enough to be removed without residue. For electrical interfaces, the advantage of printed electrodes with their low cost, thin profile, and flexibility comes alongside the challenge of maintaining a good electrical connection, especially during user motion. Past work with wearable printed electronics has made use of flexible printed cable (FPC) connectors to connect flexible electrodes to rigid readout electronics;[3,10] however, these connectors have limited lifetime connection cycles, delicate contact prongs easily damaged with mechanical strain on the connection and poor usability due to miniature latch size. Here, we make use of spring-loaded pins on the bottom of our printed circuit board for a robust, automatically-aligned connection to the printed electrodes.

On the whole, for a sweat rate monitoring device to be useful in real-world scenarios, there are several key characteristics. A device should be *wearable*–unobtrusive as well as able to function during user motion and in different environments. Minimal *dead volume*, i.e., the fluidic space between the skin and sensor, reduces the time lag between the onset of sweating and the start of sensor measurements. It can be useful to have fine *precision*, by which we refer to the minimum distinguishable increment in sweat volume, as normalized by skin collection area. *Continuous* measurements enable time-resolved analysis and real-time feedback to the user. Finally, it is important to consider *capacity*, that is, the maximum sample volume that can be measured by one sensor. Current gold standard measurement techniques for local sweat rate require trained technicians and specialized equipment and are not wearable, continuous, or both. These methods are 1) hygrometry, in which the change in temperature and water content of ventilated capsules attached to the skin are measured, and 2) gravimetry, in which the mass increase of an absorbent pad with waterproof backing adhered to an area of skin is measured.[11] Academic devices for sweat rate monitoring have explored a variety of other sensing mechanisms. Volumetric sensing, which has been validated against gold standards in several works,[2,12,13] tracks the progression of sweat through a microfluidic channel, which can be measured with computer vision processing of optical images,[13] capacitively via electrodes outside the channel,[14] or impedimetrically via electrodes inside the channel, as done here. Practically, optical images can only capture measurements at discrete timepoints, but electrodes may be used to continuously count increments in sweat volume with high precision.[2,5] Capacitive sensors may suffer from external interference from outside of the microfluidic channel, in particular, at the edge of the capacitive plates where fringing fields exist. This susceptibility presents significant challenges for the development of a robust wearable device. Further, the design of integrated measurement electronics for capacitive sensors is more challenging, with the typical magnitude of capacitance in microfluidic sensors several orders of magnitude smaller than the admittance magnitude of impedimetric sensors.[14] If these challenges can be overcome, then capacitive sensors present an interesting alternative to impedimetric sensors for potential prolonged use, as the electrodes have no contact with the sweat sample and thus are protected from electrochemical reactions and biofouling. Another method, calorimetric sensing, detects heat transfer by fluid flow from a heat source to a sensor to measure the flow rate.[8] Hygrometric sensing, as described in the previous paragraph, is also being developed in wearable form.[9] The latter two methods have theoretically unlimited capacity but may be more susceptible to environmental variables including temperature and humidity. Each method presents unique challenges, and ongoing research aims to improve their performance in real-world conditions, balancing precision, capacity, and wearability.

While wearable sweat sensing has yet to make much of a landing in the consumer market, the expansion of the field in the last decade is evidenced by the rapid rise in related academic publications and tens of millions of dollars invested in startup companies in pursuit of market-ready sensors.[15] The varied trajectories of several companies spun out of academic research labs demonstrate the challenge of developing a robust sweat-sensing product as well as the presence of a strong demand in the market for this technology. Some startups have pivoted away from aims in noninvasive fluidic sweat sensors: Biolinq out of San Diego moved to subdermal microneedle sensors for interstitial fluid, which has the advantage of higher biomarker concentrations and a more controlled environment,[16] and Kenzen, which initially made waves in heat stress sensing with several millions in funding and partnerships with professional athletics teams, pivoted to the application of existing temperature and humidity sensors.[17,18]

More recently, other companies have formed partnerships with leading groups in athletic and industrial user populations. In 2021, in partnership with Epicore Biosystems in Cambridge, MA, Gatorade released the Gx Sweat Patch, which provides a single-use, single-timepoint measurement of fluid loss. More recently, Epicore has developed the Connected Hydration product, which conducts continuous monitoring of sweating rate using interdigitated electrodes, and has partnered with Chevron to test with industrial workers.[19,20] In Boston, Nix Hydration has released a product for continuous monitoring of sweat rate and electrolyte concentration to the consumer market, using the novel technique of monitoring conductivity between two pairs of electrodes at different points in the channel and measuring flow time between the two by matching patterns in microfluctuations.[21] While there is not yet any published third-party scientific validation of the precision and robustness, the device is garnering support from several professional sports teams, including cycling powerhouse EF Pro Cycling.[22] These examples demonstrate a strong interest in wearable hydration monitoring (**Table 1**).

Today, athletes and industrial workers, who are subjected to prolonged physical exertion and high-temperature environments, rely on effective cooling and fluid regulation to maintain performance, safety, and well-being. In fact, in very different but similarly strenuous pursuits, hominins are believed to have benefited from this method of heat exchange to persistently hunt for food, to a degree that impacted their evolution.[23] In fact, due to the ability to sweat at very high rates, and the resulting heat transfer from furless skin, endurance-trained humans today have a greater capability for long-distance locomotion in hot

Table 1. Comparison of related wearable sweat rate sensor devices.

Device	Wear	Readout	Sweat rate measurement	Startup time
ELITech Macroduct[7]	Band	–	–	–
Gatorade Gx Sweat Patch[4]	Adhesive	Camera	Image processing	20–60 min
Nix Hydration Monitor	Adhesive	BLE	Pattern-matching conductivity fluctuations	Up to 25 min
Epicore Connected Hydration[19]	Adhesive	BLE	Interdigitated electrodes	Up to 60 min
Choi et.al.[14]	Adhesive LCR meter	–	Capacitive sensing	≈10 min
Kwon et al.[8]	Adhesive	BLE	Fluidic heat transport	≈3 min
Art-Sweat[5]	Adhesive	BLE	Interdigitated electrodes	≈5 min
This work	Band	BLE	Bidigitated electrodes	5–15 min

environments than nearly any other mammal, even able to outpace horses at marathon distances in the heat.[23,24] Thus, the ability to accurately measure sweat rate provides valuable insight into this unique physiological function, including hydration needs and thermal stress levels.

In the industrial sector, workers frequently face challenging conditions, such as heat exposure, heavy protective gear, and strenuous activity.[25–27] Monitoring sweat rate in such environments can help inform hydration strategies and reduce the risk of heat exhaustion, improving safety and productivity. For athletes, precise sweat rate data could enable tailored hydration strategies that can optimize performance and prevent fatigue, cramps, or more severe heat-related conditions.[28,29] Further, studies have found the sensation of thirst to be an inadequate signal for dehydration, often only occurring after a significant fluid loss has occurred, and not matching the level of fluid loss.[30] Thus, a need exists for a more accurate feedback mechanism by which fluid loss can be assessed. This also pertains to the global aging population, as older adults have a greater mismatch between thirst and fluid loss and are also more susceptible to heat stresses.[31] Therefore, precise and continuous sweat rate monitoring can serve in developing effective hydration strategies, particularly for vulnerable populations and individuals in harsh environments. As various settings present different demands, understanding sweat patterns pertaining to specific groups can help in creating specific guidelines for hydration and safety.

2. Results and Discussion

2.1. Peel-and-Stick Fluidic Interface

The collection of a sweat sample begins on the surface of the skin within the defined collection area, moves radially inward to the central bore of the skin interface, and passes through to the top face where it is directed into a disposable, peel-and-stick-replacement microfluidic sensor with ring-shaped device adhesive layer, and then continues through the spiral sensing channel to the exposed outlet. A key interface in this fluidic channel is between the reusable sweat collector and the peel-and-stick sensor layer, where sweat is directed into the sensor for detection. To join these channels without sample leakage, the device uses a layer of microfluidic adhesive, 3 M 9965 double-sided microfluidic tape. This tape has the benefit of high fluid resistance and moderately strong adhesion (reported as 21 oz in^{-1} on stainless steel) to facilitate both robust sealing and clean removal.

The skin interface is a derivative of a design which uses the form factor of a band to press a soft, concave collection well up against the skin.[2] This seals the collection area and minimizes dead volume, i.e., nonfunctional excess space in the flow channel. The well design has two main parameters: size and curvature. A greater collection area increases access to sweat glands but increases dead volume. Different sizes of collection wells are designed to optimize sweat collection, considering an individual's sweat secretion rate and desired duration or precision of measurement. For a short, high precision measurement, a large collection well would be used; for an extended measurement with a lower precision requirement, a small collection well would be used. Considering this, we adapted two sizes of collection wells with sizes of 1.14 and 3.42 cm^2 and depth of curvature between the center and raised edges of 1.57 and 2.0 mm, respectively. The inlet bores have a diameter of 0.6 mm and a total height of 2.74 mm, resulting in a dead volume of 0.8 µL. We remove alignment markings previously inset on the top of the skin interface to reduce the likelihood of sample leakage between the skin interface and the microfluidic sensor.

Repeatable sweat rate measurements are predicated on the consistency of fluid entry through the skin interface inlet and fill of the spiral microfluidic. We first verify this part in isolation from electrical measurements. To evaluate the interface of the fluidic channel between the sweat collector and single-use microfluidic, the attachment and fluid fill were tested consecutively ninety-nine times with the replacement of microfluidics each time. The results show that the interface between reusable and disposable components presents minimal discontinuity with consistent and low dead volume across many replacements.

As shown in **Figure 1**, for each of the ninety-nine trials, a microfluidic was prepared and adhered to the top face of the skin interface. Then, the skin interface was turned upside down and 10 µL of green-dyed water was injected into the base of the inlet bore by micropipette. The fill level of the microfluidic channel was recorded by optical image, and then the microfluidic was removed. The top surface of the skin interface was then wiped with an alcohol prep pad, and the process was repeated, demonstrating the reusability of the skin interface with a simple cleaning procedure.

Across all trials, the mean measured volume was 9.90 µL with a standard deviation of 0.43 µL, about 4%. Overall, the interface is robust with low variation in fluid fill. Most of the error is likely introduced at the small circular area at the start of the spiral channel, which can retain more or less fluid depending on how fluid

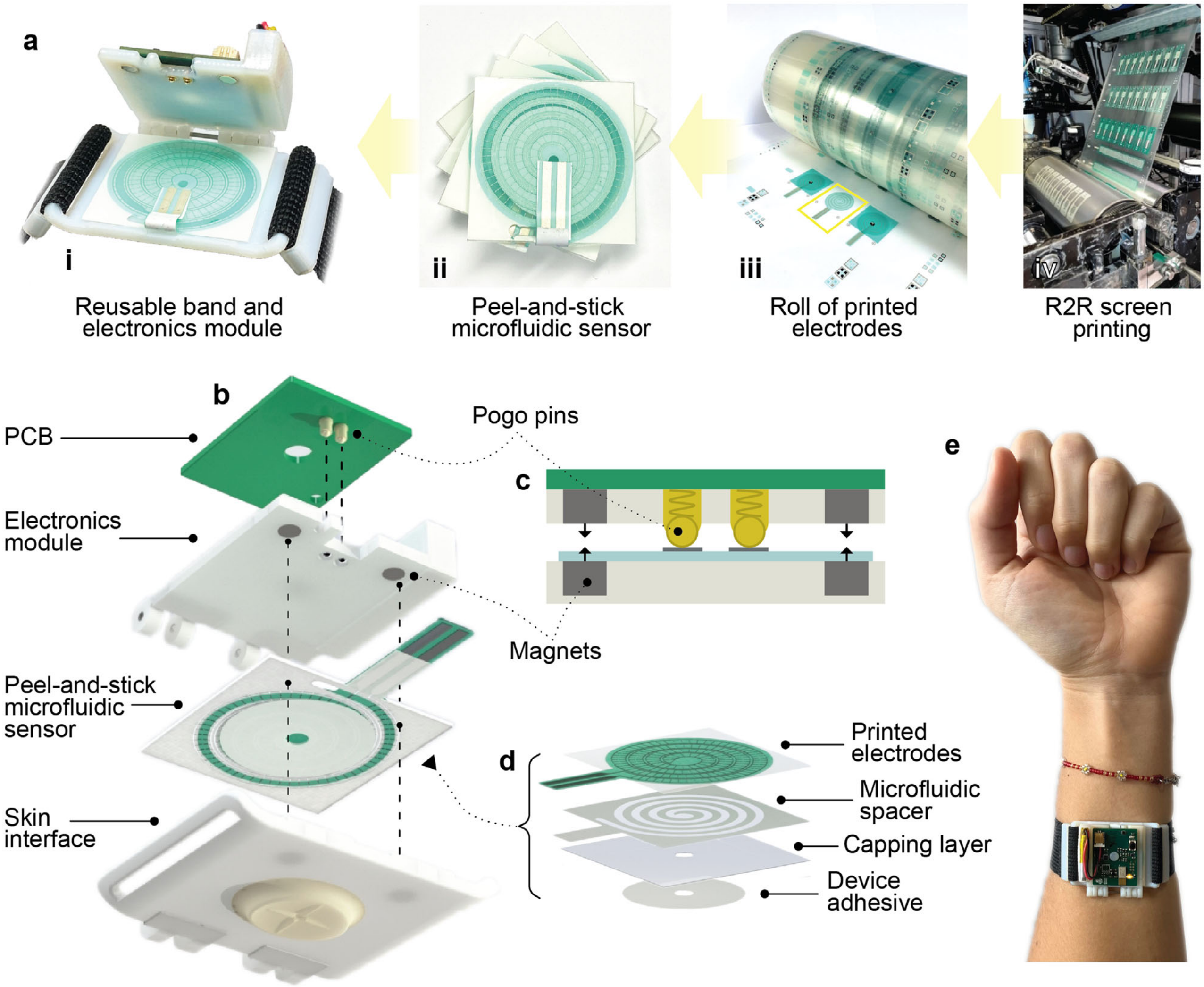

Figure 1. Overview of the precise, integrated wearable sweat rate sensor. a) (i) Photograph of the device showing the internal microfluidic sensor, (ii) multiple sensors fully assembled and cut from (iii) printed roll of electrodes, (iv) roll-to-roll screen-printing process. b) The device includes two reusable modules, the lower skin interface and upper electronics module, and a disposable microfluidic sensor. c) Cross-sectional view showing the electrical connection between the upper electronics module and single-use microfluidic sensor, made with spring-loaded pins in between pairs of rare earth magnets. d) The printed silver electrodes and microfluidic channel make up a single-use sensor that can easily be removed and replaced for each measurement. e) Photograph of the device worn on the forearm.

is drawn into the spiral channel by the hydrophilic capping layer. Some variation in the degree to which the fluid enters the channel is visible in the recorded images, some with fluid retained in the inlet and others with fluid wicked out into the spiral channel. However, this issue is alleviated in the on-body case because the channel is effectively sealed, with no air pocket in the channel behind the fluid.

2.2. Integrated Electrical Interface and Sensor Measurement

This device includes robust, fully integrated electronics for the sensor interface, sensor measurement, and data streaming. We will first discuss the electrical interface and then, building on work by,[2,3] the sensor design. To interface the printed microfluidic sensor with the circuit board, rather than using a typical flexible printed circuit (FPC) connector, which is delicate and not suited for many connection cycles, this work achieves an automatically aligned electrical connection using magnets to snap together spring-loaded pins, also known as “pogo pins,” into contact with the printed electrical pinout. We use pogo pins from Mill-Max (0965 Surface Mount Spring Loaded Pin) soldered to the bottom of the PCB. Two pairs of 3 mm diameter rare earth magnets compress the pins onto the electrode pinout and hold them in strong contact. One pair of magnets is embedded in the upper 3D-printed electronics housing, and a matching pair of magnets is embedded in the skin interface. Magnets are positioned on either side of spring-loaded pins and at maximal distance from the pivot point of the hinges, securing the closure of the device and ensuring a strong electrical connection. With the hinge closed, a gap of 300 µm between the two 3D printed submodules is left for the microfluidic

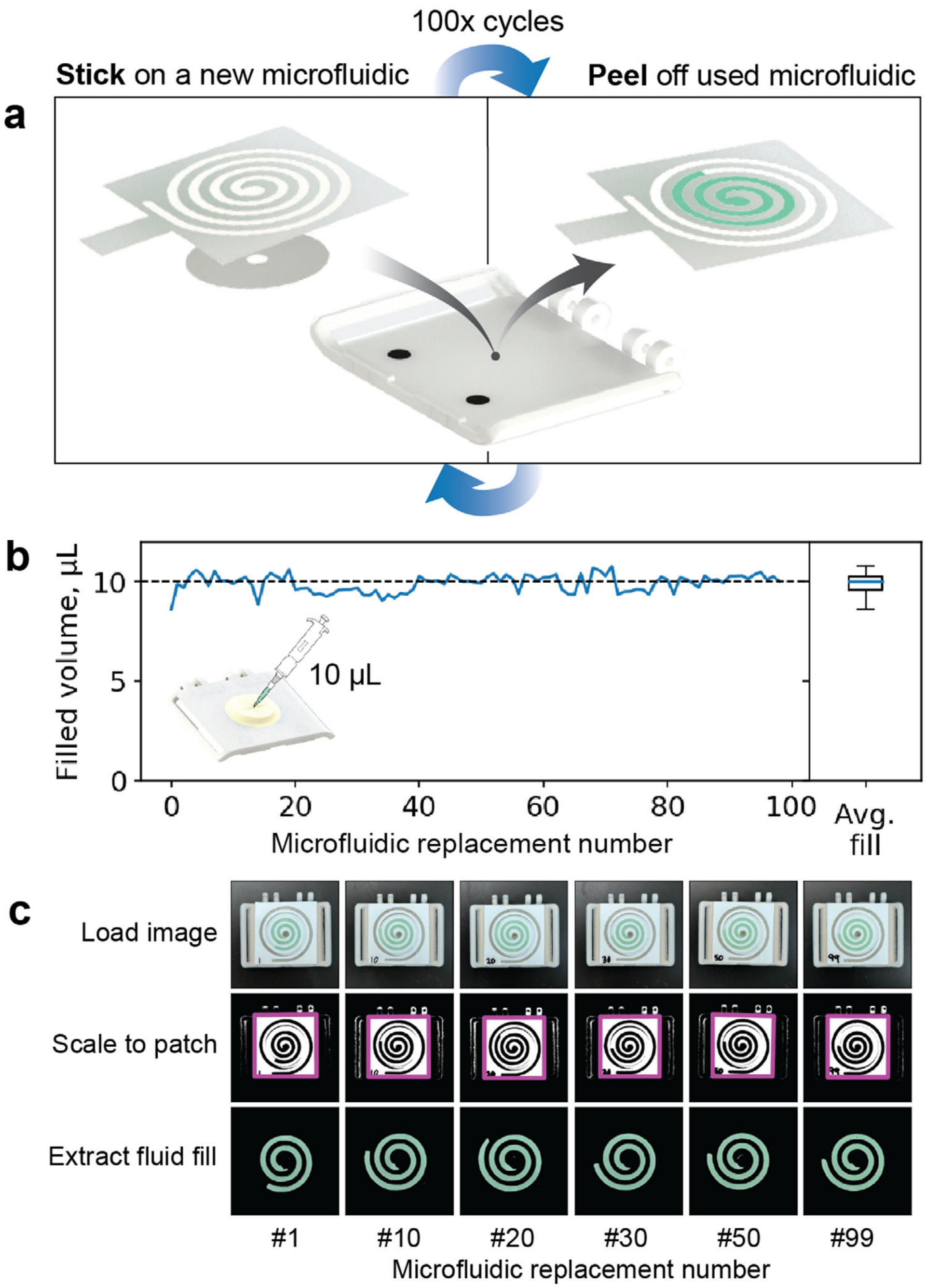

Figure 2. Repeated microfluidic connection cycles and fluid fill for each cycle. a) Process of attaching and removing microfluidic. b) Consistent volumetric fill from a series of 99 single-use microfluidics sequentially tested on the same skin interface, with mean and quartiles shown on the right. c) Images of microfluidics from select trial numbers. Here, volumetric measurement was conducted with optical images and computer image processing. Over the course of 99 microfluidic replacements, they filled to consistent volumes, with a mean of 9.90 µL and a standard deviation of 0.43 µL, demonstrating a robust fluidic interface.

sensor. Magnet placement avoids direct pressure on the fluidic channel.

We evaluate the electrical interface between the electrical submodule and disposable microfluidic sensor with one hundred sequential connections and disconnections. As the electrical submodule is released near the skin interface, it snaps into place and forms a strong electrical connection with the electrodes. To verify this, we modified the electrode of a sensor using silver ink to short the two ends of the sensor electrodes, as shown in **Figure 2**. This sensor was attached to the skin interface where it was used for the course of the measurements. Then, the resistance was measured as the electrical module with spring-loaded pins was opened and allowed to swing closed a hundred times. Each time the device was closed, the spring-loaded pins were pulled into contact with the electrodes, and the end-to-end resistance of the system was recorded, including the contact resistance of the pins as well as the resistance through the backbones of the two spiral electrodes. If the pressure on the pins were inconsistent due to weak magnetic closure or shifting of the hinge as the pivot point, we would expect to see variation in contact resistance across cycles. However, the total resistance remains consistent, validating the design of the electrical interface. The microfluidic sensor builds on a design developed in,[2,3] consisting of two printed silver electrodes tracing the length of a microfluidic channel. The two electrodes form a series of 149 gates evenly spaced along the channel. Each gate consists of a 175 μm gap between a pair of two spokes reaching into the channel from opposite sides. As the fluid front of the salty, conductive sweat sample progresses through the microfluidic channel and covers each gap in sequence, representing a volumetric increment of 160 nL, it opens this gate to the flow of electrical current. This is recorded as a stair step signal in electrical admittance magnitude. The backbones of the two electrodes are positioned just outside of the microfluidic channel, tracing its spiral pattern, and are not in contact with the sweat sample. They are designed to have a low end-to-end resistance relative to the resistance across one covered gate, with a typical printed width of 140 μm and resistance of at most 150 Ω which is measured in series with the 15–20 kΩ contribution of each gate crossing. As a result, even with this "lead resistance," the last gates on the electrode backbone contribute similar admittance to the gates nearest to the electrical pinout.

The raw signal from the microfluidic looks like a set of stairs, as shown in Figure 2f, ideally with a flat baseline superimposed by a series of nearly vertical jumps in electrical admittance occurring upon each gate crossing. To process this signal, the number of gate crossings is counted in uniform time intervals (we use 1 min), and then each count is converted to a corresponding fluid volume and used to determine the average flow rate for that interval of time.[2,3] Sensor calibrations are done for 1–10 μL min^{-1} flow rates using a controlled flow pump with mock sweat solution including the full physiological range of 10–100 mM sodium chloride.[32] This data is shown in Figure 2g and the testbed in Figure S3 (Supporting Information). In this system, the main challenge is designing the system to read out clear, distinct steps upon gate crossings, despite variations in the ion content and flow profile of the sweat sample. The sharpness of the vertical rises depends on how quickly and fully the progressing fluid front covers the gate's primary connecting area, which can be optimized by the electrode geometry. In order to stabilize this signal even for nonideal flow profiles where the fluid front is uneven, which can occur for example upon shaking the microfluidic, we use digitate electrodes, spaced in pairs with small gaps in between, rather than alternating interdigitated electrodes.

Returning to the staircase analogy, the flatness of the steps depends on the parameters of the electrical measurement. While the sensor electrodes can be simply modeled as a set of parallel resistors representing each gate crossing, with the electrochemical nonidealities of the system, there are more and less optimal methods of measuring the electrical admittance signal. The excitation voltage should have sufficiently low amplitude; voltages in excess of a few hundred millivolts cause signal drift due to chemical reactions between the silver electrodes and the sweat sample. Figure S5 (Supporting Information) shows the measured drift of the effective conductance between sensor electrodes when applying DC voltage and the channel filled with a 50 mM NaCl mock sweat solution. With increasing voltage levels, there is a larger drift in conductance due to the reactivity of silver, in particular reacting to form silver chloride. Also seen in this figure is that with DC excitation voltage, there is continual drift due to electrode surface changes and solution polarization. Therefore, the excitation voltage should not be constant but instead alternating, with a sufficiently high frequency. Accordingly, we designed a measurement circuit to generate an excitation signal of frequency 50 kHz and amplitude 270 mV for measurement of admittance magnitude.

To verify the measurement electronics for the sensor, which are expected to read out electrical admittance magnitude, the board was calibrated on discrete resistors. As shown in Figure 2, the measurement channel is precise enough to measure the step height for a single gate crossing with a sweat sample, ≈50 μS increments in admittance. The measurement channel is also very linear up to ≈11 mS, which is well above the final admittance reached with all gates connected in a full channel.

2.3. Fully Wearable On-Body Sweat Rate Monitoring

Overall, the sensor system measures 41 mm × 34 mm × 9.95 mm (V = 13.9 cm^{3}) and weighs 8.8 g without the band, comparable in size to commercial smartwatches. For example, the Apple Watch Series 10 (42 mm version) measures 42 mm × 36 mm × 9.7 mm and weighs 30 g.

The device was evaluated in on-body experiments with both heat- and exercise-stimulated sweating across different times of day. The experimental results are shown in **Figure 3**. The sweating rate was monitored on either the left or right forearm, or both. For cycling experiments, a smart indoor bike trainer was used to monitor the power output from the cyclist. Temperature was also recorded using a temperature sensor worn on the arm.

In high-temperature environment trial (a), where the subject was sedentary but the temperature hovered ≈35 °C, the sweat rate ranged from 0.1–0.4 μL min^{-1}cm^{-2}. In the cycling trials, the subject exercised with power output in steps of different wattage. Sweat rates ranged from 0.21.0 μL min^{-1}cm^{-2}, with higher values during periods of higher power output. In trials (b)–(c), sweat rate was measured on both left and right arms. Aside from slightly different times for the start of sensor measurements, the right and left sides track well against each other. This consideration of whether sweat rate measurements correlate as expected across left and right arms and with physiological and environmental parameters provides some standalone validation of the sensor response. The measured sweat secretion rate is consistently elevated during levels of physical activity or elevated temperature, compared to periods of rest. The separate periods of high and low exercise rates further demonstrate the system's ability to monitor a range of sweating rates on the body and affirm the relative changes that are reported. In trials (d)–(f), longer measurement durations (≈40 min) during high sweating rate were enabled by the use of the smaller, 1.1 cm^{2} collection well, instead of the 3.4 cm^{2} well used in the other trials.

Across all trials, the average time to begin receiving sensor measurements from the start of exercise is just under 10 min.

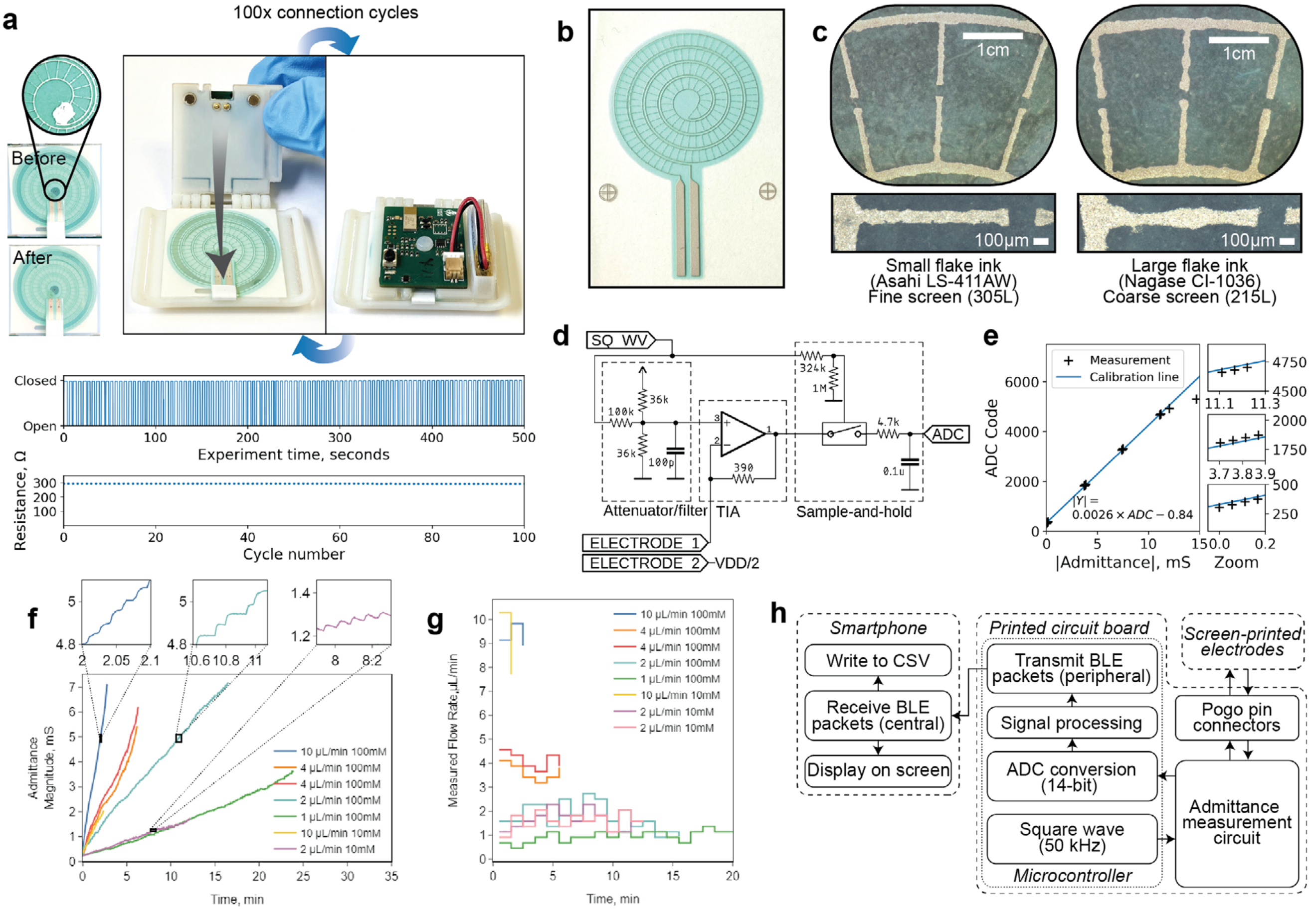

Figure 3. Design and verification of integrated measurement electronics. a) Repeated PCB/electrode connection cycles and net resistance measurement for each cycle. The connection is made via magnets pressing down springloaded pins onto the pinout of the printed electrodes. The measured resistance consists of the end-to-end resistance of the two interdigitated electrodes in series and the contact resistance between the spring-loaded pins and printed electrodes. Over the course of 100 connection cycles, neither contact resistance nor electrode resistance is significantly raised. b) Electrode pattern via silk screen printing on TPU. c) Magnified optical images of designs printed with LS-411 W and CI-1036 silver inks. The LS-411 W is printed with fine mesh silkscreen, 305 lines per square inch, and produces sharper patterns. d) Admittance measurement circuit with configurable excitation signal amplitude, transimpedance amplifier, and analog switch-based sample-and-hold detection. The output is a voltage read by the ADC of the microcontroller e) Calibration of the admittance measurement channel with discrete resistors. The spacing between close measurement points was chosen to match the magnitude of a single gate crossing in the sensor. f) Raw admittance signal from benchtop calibrations with flow pump injection of 10, 4, 2, 1 µL min^{-1} in 100 or 10 mм NaCl with expanded views of steps and g) reconstructed flow rate for each measurement. h) Block diagram of full measurement system used for all admittance measurements in the paper.

Trials (c) and (d) took the least amount of time to begin measurements, only 5–7 min, as might be expected with the highest temperature and work rate. The sensor measurement startup time is the point when the first gate in the microfluidic channel is crossed by the sweat sample, depending on the individual's onset and rate of sweating as well as the device's dead volume. In this device, this occurs after enough sweat has collected in the skin interface to be pushed up into its inlet, and then to emerge from the inlet, requiring a certain burst pressure, and travel a small way into the spiral microfluidic. Differences in start times between the left and right sides may have to do with small differences in dead volume across devices and movement-induced break of the burst pressure required to begin the fill of the microfluidic. Note that the sudden initial increase in sweat rate seen in each trial has to do with the small dead volume present in the fluidic channel between the skin and the first electrode gate.

The more gradual initial sweating rates as the subject begins to warm up or exercise are not detected until sufficient sweat has first filled this dead volume. However, after the dead volume has filled and the first electrode gate has been crossed, low sweat rates are able to be measured, as shown in the periods of light exercise in Figure 3. In trials (c)–(e), a decrease in exercise power output was consistently followed by a drop in sweat rate of ≈0.4 µL min^{-1}cm^{-2}, with only a few minutes delay between these events. The consistent increase in sweat rate across all trials after the initiation of exercise, along with the decrease in sweat rate in select trials where exercise power output was stepped down demonstrates a strong correlation between exercise and sweat rate for both short (≈20 min) and long trials (≈60 min).

One limitation of volumetric microfluidic sensors is the capacity; the sensors in this work measure up to 23.8 µL.

At a moderately high sweating rate of 0.5 µL $\min^{-1}\mathrm{cm}^{-2}$, this supports up to 42 active minutes of monitoring, possibly interspersed with periods of low sweat rate or rest, using a 1.1 cm^2 area collection well. In this design, the length and width of the microfluidic channel are constrained by the overall form factor of the device, as described in Figure S1 (Supporting Information), whereas the channel height is kept small in order to prevent motion artifacts in the fluid flow.

However, with a simple replacement of the microfluidic sensor, this work enables prolonged measurements with consistent volumetric precision. Trial (f) shows the replacement of the microfluidic sensor in real-time. During a pause in cycling, the subject removed the device, opened the hinge, and replaced the first sensor with a new one, wiping the surface with an alcohol pad in between. Sensor measurements quickly resumed with only 11 min total interruption, attesting to the low dead volume of the microfluidic and the simplicity and reliability of the interfaces for short or long-term monitoring.

2.4. Future Work

This section discusses some of the present limitations of the device and possible design changes for future iterations. One issue encountered is backflow in the microfluidic system after a period of inactivity, possibly due to absorption and evaporation from the skin. This is not problematic on its own, simply resulting in a downward stepping in the admittance signal, but the prewetting of the channel can alter subsequent fluid flow and reduce the accuracy of collected data. Additionally, variations in the tightness of the device's band–sometimes caused by muscle flexion–can create a pumping effect. These changes in pressure in the microfluidic channel may lead to air bubbles and possible artifacts in the measurement. These fault cases can be avoided if the subject moves carefully, but the investigation could work toward enabling a wider scope of on-body measurements.

Another area for refinement lies in the design of the electrodes. Modifying the electrode layout to have smaller exposed gate areas, for example, by printing an insulating layer over their interconnects nearly all the way up to the junction, could make the gate crossing signal more discrete. This could improve the robustness of signal detection, especially under irregular fluid flow due to conditions such as those described in the previous paragraph.

Adding onboard data storage to the band itself would allow for continuous data collection even when the user is away from their mobile phone. This feature would be particularly valuable for users engaging in long-term monitoring where constant proximity to their smartphone may be undesirable, thereby improving the device's overall robustness and versatility.

Finally, conducting broad experiments across many individuals from different age groups, genders, body types, and sweating rates could lead to more generalizable conclusions about the onset time of sweating and sensitivity of sweat rates to different work rates and environments, or establish methods for personalized hydration analysis.

3. Conclusion

In conclusion, this system represents a significant advancement in wearable sweat rate monitoring technology. Integrating microfluidics, printed electronics, and wireless measurement with simple, reliable interfaces, the device achieves precise and continuous, real-time sweat rate analysis. The modular design of reusable and disposable components with peel-and-stick-replacement microfluidics and spring-loaded electrical connections facilitates ease of use while maintaining measurement accuracy. On-body testing demonstrates the system's capability to inform hydration strategies during cycling and environmental heat stress. Despite current limitations on device usage to avoid backflow and pumping in the microfluidic system, ongoing improvements to the electrode design aim to improve reliability and versatility. Ultimately, this work holds promise for widespread applications in sports science, occupational health, and beyond, contributing valuable physiological insights for safety and performance in an emerging dimension of wearable sensors.

4. Experimental Section

Microfluidic: The microfluidic channel is composed of three layers, as shown in **Figure 4**: a microfluidic spacer with a spiral flow channel sandwiched between a printed electrode layer and a capping layer. The microfluidic spacer was laser cut from 3M 9965, a double-sided white tape with hydrophobic acrylate adhesive and a thickness of 86 µm. The capping layer was laser cut from 3M 9984, a polyester film with hydrophilic coating on one side, which was oriented to face the inside of the channel.

Laser patterning was done on a Universal Laser Systems PLS4.75 CO2 laser cutter.

Lamination of these layers was done by hand with help from crosshair alignment markings in the printed electrodes and fluidic layer. The layers were annealed on a hot plate at 90 °C for 5 min to soften the adhesive and then firmly pressed together with a craft seam roller.

Printed Electrodes: The electrode layer was fabricated in a scalable manner using roll-to-roll (R2R) screen printing.

To produce sensing electrodes, a roll of thermoplastic polyurethane (TPU) substrate (Platilon U073, 100 µm thick) was laminated to a PET carrier foil (75 µm thick), and thermally pretreated (oven at 140 °C, dwell time ≈1.8 min) before sequential roll-to-roll rotary silk screen printing of 1) structural dielectric layer (Loctite EDAG 452SS, screen mesh count 305L, UV cured, 4 m $\min^{-1}$), and 2a) silver conductive tracks (Asahi LS-411AW, screen mesh count 305L, oven-dried at 120 °C, 2 m $\min^{-1}$, drying time ≈3 min), or 2b) silver conductive tracks (Nagase ChemteX CI1036, screen mesh count 215L, oven dried 120 °C, 2 m $\min^{-1}$, drying time ≈3 min). Printed layers were manually registered, with the alignment monitored using a camera module mounted on the printing line.

Two different silver inks were tested in the printing process, a standard silver ink for screen printing (Asahi LS-411 W) and a silver ink developed especially for durability under creasing and stretching (Nagase CI-1036). The CI-1036 had larger flakes of silver and was thus printed using a coarser mesh silkscreen (215L) to allow the ink to pass through. On the other hand, the LS-411 W had finer silver particles and could be printed with a fine mesh silkscreen (305L), allowing for more precisely resolved patterns.

Sensor Measurement: In order to have more control over the measurement, rather than use commercial analog front-end ICs with impedance measurement capabilities (e.g., Analog Devices AD5940), a simple custom measurement channel was built for admittance magnitude. To minimize power consumption and footprint, the circuit eliminates the need for a DAC to produce the needed 50 kHz excitation waveform. Instead, it takes a square wave of the desired frequency directly from a timer output on the microcontroller and then uses a simple RC network to attenuate and filter this to the desired amplitude and shape. This voltage waveform

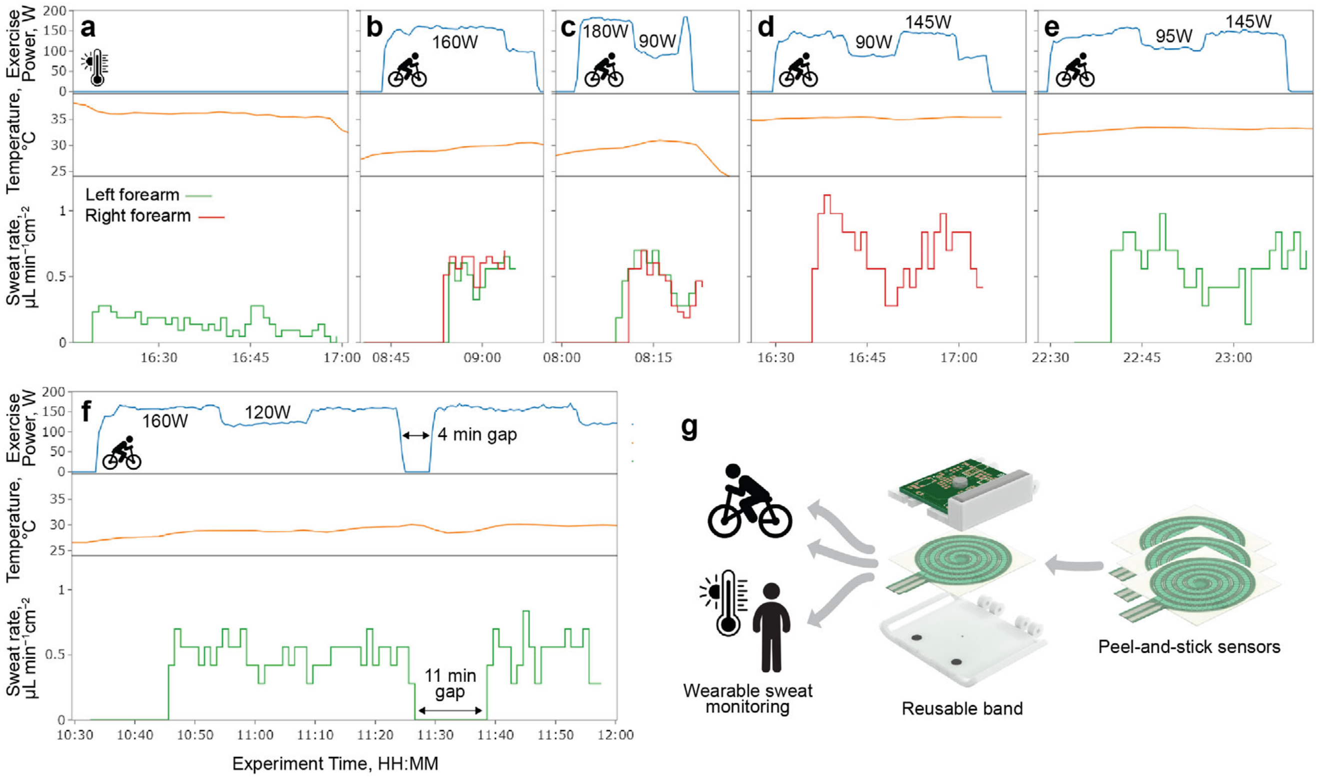

Figure 4. On-body data was collected with the sensor system. Experiments include a) sedentary in a hot environment and b–e) indoor cycling on a smart bicycle trainer. The top row shows the exercise power output of the subject, the middle row the environmental temperature, and the bottom row the measurements from sensors worn on either the left or right forearm, or both. Cycling periods with near-constant power output are annotated on the plots. f) On-body data demonstrating a "hot swap" of microfluidic sensor mid-exercise. The time taken to replace the sensor was 4 min, and the total gap in the measurement was 11 min, including some time to resume cycling and sweating, demonstrating the ease of use and the robustness of the interfaces. g) Schematic of device usage.

was then applied between the two sensor electrodes and the resulting current was read out with a transimpedance amplifier. Finally, a switch-based sample-and-hold circuit was used to measure the positive peaks of the oscillating signal, extracting the DC amplitude. The switch was controlled by a filtered branch of the same square wave driving the excitation signal, allowing it to sample the positive half of each period of the AC output in synchronization. To form the control signal, the square wave was passed through a high-valued resistor divider in combination with parasitic capacitance to cross the 70–30% high-low switch control voltages in a narrowed window. In theory, this control signal could be tuned to sample other portions of the output waveform. Finally, the sampled peaks of the AC output were stabilized over a lowpass filter and fed to an analog input of the microcontroller.

This measurement was calibrated with discrete resistors and had a high precision of up to 11mS, as shown in Figure 2.

Wireless Data Communication: Sensor electronics and an accompanying mobile app were designed to stream sensor data continuously and in real-time. Bluetooth Low Energy (BLE) was selected as the communication protocol due to its energy efficiency, capability to support a large number of sensor nodes, and broad compatibility.

This section discusses the BLE chipset selection, the structure, and frequency of the data packets used to transmit measurements from the sensor devices, as well as the development of the accompanying mobile application for the display and storage of data.

For BLE communication, a wireless module with a 2.4 GHz radio was used in the sensor device. The EYSHSNZWZ module from Kaga Fei was selected, as it was built on a Nordic Semiconductor nRF52832 system-on-chip, includes a system clock and antenna, and measures only 3.25 mm × 8.55 mm × 0.9 mm.

The sensor device transmits sensor measurements in batches of eight via BLE notification to the central device after a connection had been established. The transmissions were made with a radio power of +4 dBm. With a relatively quick sensor data interval of 200 ms, measurements were collected into a group before transmission for efficiency. The data payload contains one byte of flags, a 2-byte sequence number, and then eight 16-bit integer measurements (a total of 19 bytes). This was the maximum number of measurements that would fit into a BLE data packet when using the default Attribute Maximum Transmission Unit (ATT MTU) of 23 bytes, which had three bytes reserved for the opcode and attribute handle header.

BLE offers two methods, notifications and indications, for transferring data from a peripheral device (sensor node) to a central device (mobile phone). Notifications were used–the method with higher throughput capability and lower power consumption. While the following point was sometimes confused, both methods did allow the peripheral device to confirm the reception of data packets. While indications involved an acknowledgment of data reception from the central device's application layer, notifications also received an acknowledgment but only from the link layer. In this case, there was no need for application-level acknowledgment, so the more efficient option, notifications was chosen.

Finally, while the sensor device relied on streaming to save data and did not have onboard data logging, in the event of a dropped wireless connection, data packets were added to a queue in RAM and then transmitted upon reconnection. This solution could be improved, e.g. storing the queue in flash memory, of which the microcontroller had 512 kB, rather than RAM, which was only 64kB and nearly full with program variables, to allow for a larger queue size and persistence across power loss. Even in this iteration, however, the queue accounts for temporary loss of connection without data loss.

A mobile app was also developed to receive data from sensor devices and was able to plot and store the data in real-time. The user could export the data to CSV files for further analysis. In addition, the app allows the user to connect to multiple devices at the same time with a maximum number of ≈12 devices, depending on the phone's Bluetooth capabilities. Each device could be disconnected and reconnected at any time without affecting the other devices' connection, allowing flexible and dynamic experiments. Data received from each device was stored in a separate file and plotted on the same graph. The app was developed using Swift and Xcode, and it communicates with the sensor devices using Bluetooth Low Energy (BLE) technology.

The data communication was evaluated by wearing multiple sensors on different skin sites and measuring the received signal strength indicator (RSSI) during the BLE advertisement. In practice, the mobile app could connect up to at least twelve sensor nodes at once. With a limited number of available sensor nodes, the communication signal strength was tested with three. With one sensor on each forearm as well as one on the left bicep, a subject tested three different scenarios–walking with the phone in a pants pocket, indoor cycling with the phone positioned in front of the bicycle close to the handlebars, and indoor cycling with the phone worn in a jersey pocket on the back. The RSSI for these cases is plotted in Figure S6 (Supporting Information). It was well known that antenna performance could behave strangely in close proximity to the human body, which might account for the relatively low signal strength seen by the phone. However, the signal was quite strong in the second case with the phone positioned in front of the stationary bicycle, and with onboard data buffering, sufficient to stream data with only 0.2–0.7% packet loss for sensors on the right and left forearm in a similar experiment lasting 40 min.

Power: Power was supplied with a classic LiPo battery, which was rechargeable with a 3.7 V output. The power consumption is shown in Figure S6 (Supporting Information), with a mean current draw was 6.2 mA, and a mean power consumption of 23 mW. For sensor readings, the ADC was oversampled at an interval of 2 ms, while data packets were transmitted to the phone at an interval of 200 ms. These two events caused brief spikes of ≈10 and ≈30 mA in the current draw, respectively, and overall had a small effect on the mean current draw, which remains close to the 5.5 mA baseline. Using the smallest commercially available LiPo battery at this time, 40 mAh, the lifetime of the sensor device was 6.5 h.

Skin Interface and Packaging: The skin interface and electronics module each had two hinges, with one possessing a soft inner grip that holds onto the hinge pin, and a 1 mm diameter stainless steel wire, connecting the two parts. The submodules further had magnets secured in place with super glue, an outlet hole aligned with the fluidic outlet on the fluidic microchannel, a battery holder, and a PCB holder. For waterproofing, the PCB was coated in a layer of clear fingernail polish.

The skin interface and electronics module were printed on an Objet260 polyjet 3D printer using the proprietary materials Agilus30 Clear, RGD515 Digital ABS, and RGD531 Digital ABS, which were combined in different ratios to provide a wide range of rigidity, and water-soluble support material (FullCure705). The soft, deformable collection well of the skin interface was printed with Agilus30 Clear, which allows the skin to press comfortably into its curved surface and for a good watertight seal. The base of the skin interface, the electronics module, and the hinges were all printed with a 2:1 mixture of RGD531 and RDG515 digital ABS characterized by greater rigidity. After printing, the support material was removed using hand tools and a water jet. The inlet hole of the collection well was further cleaned with a 1 mm diameter needle and isopropanol alcohol.

Data Processing: The raw electrode admittance data was processed with a Python script to report the sweat rate. After identifying the gate crossings, the number of gate crossings in each 1 min interval was used to calculate an average sweat rate for that time period to produce the results plotted in Figures 1 and 2.

Controlled Flow Rate Characterization: The controlled flow rate characterization was conducted with a NE-1000 syringe pump (Pump Systems Inc.) The syringe needle was inserted into the inlet of the skin interface and sealed with hot glue. The testbed is shown in Figure S3 (Supporting Information). Flow rate measurements were read out by the custom PCB and paired custom iPhone application.

On-Body Sweat Analysis: On-body human trials were carried out in compliance with the human research protocol (CPHS 2014-08-6636) approved by the Institutional Review Board (IRB) at the University of California, Berkeley. Informed consent was obtained from the subject before enrollment in the study. For the stationary cycling trials, the subject rode on a road bicycle mounted to a smart trainer (Elite Direto XR-T Smart Trainer). Sweat rate measurements were read out by the custom PCB and paired custom iPhone application. In addition to monitoring sweat rate on-body, temperature was also tracked, using a separate BME688 environmental sensor reporting at 2 Hz, shown in Figure S7 (Supporting Information).

Supporting Information

Supporting Information is available from the Wiley Online Library or from the author.

Acknowledgements

This work was supported by the Berkeley Sensors and Actuators Center (BSAC), and Samsung Electronics. The contribution from VTT was supported by The Academy of Finland (Grant No. 351282). Part of the facilities at VTT was funded by the Academy of Finland Research Infrastructure "Printed Intelligence Infrastructure" (PII-FIRI, Grant No. 320020). Technical assistance from Jari Rekilä (layout for screen printing), Hannu Sääskilahti (R2R screen printing), Ashwin Aggarwal (signal processing script), and Luis Fernando Ayala-Cardona (design for skin interface) is gratefully acknowledged. N.D. acknowledges support from the National Defense Science and Engineering Graduate (NDSEG) Fellowship Program, and A.K. acknowledges support from the Bakar Ignite Scholars Program.

Conflict of Interest

The authors declare no conflict of interest.

Data Availability Statement

The data that support the findings of this study are available from the corresponding author upon reasonable request.

Keywords

printed electronics, sweat rate, system integration, wearable computing

Received: March 7, 2025
Revised: April 21, 2025
Published online:

---

[1] L. B. Baker, C. T. Ungaro, B. C. Sopena, R. P. Nuccio, A. J. Reimel, J. M. Carter, J. R. Stofan, K. A. Barnes, *J. Appl. Physiol.* **2018**, *124*, 1304.
[2] M. Dautta, L. F. Ayala-Cardona, N. Davis, A. Aggarwal, J. Park, S. Wang, L. Gillan, E. Jansson, M. Hietala, H. Ko, J. Hiltunen, A. Javey, *Adv. Mater. Technol.* **2023**, *8*, 2201187.
[3] M. Bariya, N. Davis, L. Gillan, E. Jansson, A. Kokkonen, C. McCaffrey, J. Hiltunen, A. Javey, *ACS Sens.* **2022**, *7*, 1156.
[4] L. B. Baker, A. S. Wolfe, *Sports Sci. Exchange* **2022**, *35*, 234.
[5] M. Liu, S. Liu, T. Zhang, D. Zhou, L. Li, Q. Gao, Y. Liu, C. Ge, Y. Wang, M. Wang, F. Wen, Z. Xiong, Z. Zhou, S. Wang, T. Zhang, *Biosens. Bioelectron.* **2024**, *257*, 116299.

[6] Macroduct Sweat Collection System (Model 3700) Instruction/Service Manual, Wescor, Inc., Utah **2004**.
[7] G. Matzeu, C. Fay, A. Vaillant, S. Coyle, D. Diamond, in *IEEE Transactions on Biomedical Engineering*, Piscataway, NJ, USA August **2016**.
[8] K. Kwon, J. U. Kim, Y. Deng, S. R. Krishnan, J. Choi, H. Jang, K. Lee, C.-J. Su, I. Yoo, Y. Wu, L. Lipschultz, J.-H. Kim, T. S. Chung, D. Wu, Y. Park, T.-i. Kim, R. Ghaffari, S. Lee, Y. Huang, J. A. Rogers, *Nat. Electron.* **2021**, *4*, 302.
[9] A. Aggarwal, M. Dautta, L. F. Ayala-Cardona, A. Wudaru, A. Javey, *Adv. Mater. Technol.* **2023**, *8*, 2300385.
[10] W. Gao, S. Emaminejad, H. Y. Y. Nyein, S. Challa, K. Chen, A. Peck, H. M. Fahad, H. Ota, H. Shiraki, D. Kiriya, D.-H. Lien, G. A. Brooks, R. W. Davis, A. Javey, *Nature* **2016**, *529*, 509.
[11] L. B. Baker, *Sports Med.* **2017**, *47*, 111.
[12] H. Y. Y. Nyein, L.-C. Tai, Q. P. Ngo, M. Chao, G. B. Zhang, W. Gao, M. Bariya, J. Bullock, H. Kim, H. M. Fahad, A. Javey, *ACS Sens.* **2018**, *3*, 944.
[13] L. B. Baker, J. B. Model, K. A. Barnes, M. L. Anderson, S. P. Lee, K. A. Lee, S. D. Brown, A. J. Reimel, T. J. Roberts, R. P. Nuccio, J. L. Bonsignore, C. T. Ungaro, J. M. Carter, W. Li, M. S. Seib, J. T. Reeder, A. J. Aranyosi, J. A. Rogers, R. Ghaffari, *Sci. Adv.* **2020**, *6*, abe3929.
[14] D.-H. Choi, M. Gonzales, G. B. Kitchen, D.-T. Phan, P. C. Searson, *ACS Sens.* **2020**, *5*, 3821.
[15] N. Davis, J. Heikenfeld, C. Milla, A. Javey, *Nat. Biotechnol.* **2024**, *42*, 860.
[16] W. Jia, A. J. Bandodkar, G. Valdés-Ramírez, J. R. Windmiller, Z. Yang, J. Ramírez, G. Chan, J. Wang, *Anal. Chem.* **2013**, *85*, 6553.
[17] S. Buhr, Kenzen wins for best startup in the future athlete category at the NFL's 1st and future **2016**, https://techcrunch.com/2016/02/06/kenzen-wins-for-best-startup-in-the-future-athlete-category-at-the-nfls (accessed: November 2024).
[18] N. E. Moyen, R. C. Bapat, B. Tan, L. A. Hunt, O. Jay, T. Mundel, *Int. J. Environ. Res. Public Health* **2021**, *18*, 13126.
[19] J. C. Spinelli, B. J. Suleski, D. E. Wright, J. L. Grow, G. R. Fagans, M. J. Buckley, D. S. Yang, K. Yang, S. M. Beil, J. C. Wallace, T. S. DiZoglio, J. B. Model, S. Love, D. E. Mac- intosh, A. P. Scarth, M. T. Marrapode, C. Serviente, R. Avila, B. K. Alahmad, M. A. Busa, J. A. Wright, W. Li, D. J. Casa, J. A. Rogers, S. P. Lee, R. Ghaffari, A. J. Aranyosi, *npj Digital Med.* **2025**, *8*, 1.
[20] M. Stewart, A. Tineo, B. Woodrow, M. Wasik, S. Chan, *Artificial Intelligence, Social Computing and Wearable Technologies* (Eds: W. Karwowski, T. Ahram), AHFE Open Access, USA, **2023**.
[21] Nix Hydration Biosensor Science and Validation, https://nixbiosensors.com/pages/nix-hydration-biosensor-science-and-validation-research-and-development (accessed: November 2024).
[22] Nix Biosensors and EF Pro Cycling team up, https://efprocycling.com/culture/nix-biosensors-and-ef-pro-cycling-team-up/ (accessed: November 2024).
[23] D. E. Lieberman, *Comprehensive Physiology*, John Wiley & Sons, Ltd., Hoboken, NJ, USA **2014**, pp. 99–117.
[24] D. E. Lieberman, D. M. Bramble, *Sports Med.* **2007**, *37*, 288.
[25] T. M. McLellan, G. A. Selkirk, *Ind. Health* **2006**, *44*, 414.
[26] D. J. Brake, G. P. Bates, *Occup. Environ. Med.* **2003**, *60*, 90.
[27] R. M. Morgan, M. J. Patterson, M. A. Nimmo, *Acta Physiol. Scand.* **2004**, *182*, 37.
[28] M. F. Bergeron, *J. Sci. Med. Sport* **2003**, *6*, 19.
[29] S. J. Montain, W. A. Latzka, M. N. Sawka, *J. Appl. Physiol.* **1995**, *79*, 1434.
[30] D. B. Engell, O. Maller, M. N. Sawka, R. N. Francesconi, L. Drolet, A. J. Young, *Physiol. Behav.* **1987**, *40*, 229.
[31] G. W. Mack, C. A. Weseman, G. W. Langhans, H. Scherzer, C. M. Gillen, E. R. Nadel, *J. Appl. Physiol.* **1994**, *76*, 1615.
[32] L. B. Baker, *Temperature* **2019**, *6*, 211.